Simulation of shallow water jets with a unified element-based continuous/discontinuous Galerkin model with grid flexibility on the sphere

S. Marras*, M. A. Kopera, F. X. Giraldo

Department of Applied Mathematics, Naval Postgraduate School

*Correspondence to: 833 Dyer Road, Bldg. 232, Spanagel 249A, Monterey, CA 93943 U.S.A.

smarras1@nps.edu; fxgirald@nps.edu

We test the behavior of a unified continuous/discontinuous Galerkin (CG/DG) shallow water model in spherical geometry with curved elements on three different grids of ubiquitous use in atmospheric modeling: (A) the cubed-sphere, (B) the reduced latitude-longitude, and (C) the icosahedral grid. Both conforming and non-conforming grids are adopted including static and dynamically adaptive grids for a total of twelve mesh configurations. The behavior of CG and DG on the different grids are compared for a non-linear mid-latitude perturbed jet and for a linear case that admits an analytic solution. Because the inviscid solution on certain grids shows a high sensitivity to the resolution, the viscous counterpart of the governing equations are also solved and the results compared. The logically unstructured element-based CG/DG model described in this paper is flexible with respect to arbitrary grids. However, we were unable to define a best grid configuration that could possibly minimize the error regardless of the characteristic geometry of the flow. This is especially true if the governing equations are not regularized by the addition of a sufficiently large, fully artificial, diffusion mechanism, as will be shown. The main novelty of this study lies in the unified implementation of two element-based Galerkin methods that share the same numerical machinery and that do not rely on any specific grid configuration to solve the shallow water equation on the sphere.

Key Words: Reduced Lat-Lon grids; Icosahedral Grid; Cubed-Sphere; Shallow Water Equations; Galerkin Methods; Spectral Element; Discontinuous Galerkin; Barotropic Jet; Galewsky Flow; Grid Generation on

 Prepared using qjrms4.cls

Report Documentation Page

Form Approved
OMB No. 0704-0188

1. REPORT DATE	2. REPORT TYPE	3. DATES COVERED
2013		**00-00-2013 to 00-00-2013**

4. TITLE AND SUBTITLE	5a. CONTRACT NUMBER
Simulation of Shallow Water Jets with a Unified Element-based Continuous/discontinuous Galerkin Model with Grid Flexibility on the Sphere	5b. GRANT NUMBER
	5c. PROGRAM ELEMENT NUMBER
6. AUTHOR(S)	5d. PROJECT NUMBER
	5e. TASK NUMBER
	5f. WORK UNIT NUMBER
7. PERFORMING ORGANIZATION NAME(S) AND ADDRESS(ES) **Naval Postgraduate School,Department of Applied Mathematics,Monterey,CA,93943**	8. PERFORMING ORGANIZATION REPORT NUMBER
9. SPONSORING/MONITORING AGENCY NAME(S) AND ADDRESS(ES)	10. SPONSOR/MONITOR'S ACRONYM(S)
	11. SPONSOR/MONITOR'S REPORT NUMBER(S)

12. DISTRIBUTION/AVAILABILITY STATEMENT
Approved for public release; distribution unlimited

13. SUPPLEMENTARY NOTES

14. ABSTRACT

15. SUBJECT TERMS

16. SECURITY CLASSIFICATION OF:			17. LIMITATION OF ABSTRACT	18. NUMBER OF PAGES	19a. NAME OF RESPONSIBLE PERSON
a. REPORT	b. ABSTRACT	c. THIS PAGE			
unclassified	**unclassified**	**unclassified**	**Same as Report (SAR)**	**21**	

1. Introduction

As computational power increases, meteorologists demand greater resolution from global atmospheric models utilizing spherical domains. Driven by the need to select the most proper computational grid on the sphere for the *Nonhydrostatic Unified Model of the Atmosphere* (NUMA) (Kelly and Giraldo 2012; Giraldo *et al.* 2013), in this paper we analyze the continuous Galerkin (CG or *spectral element(s)*, from now on) and discontinuous Galerkin (DG) solutions of the shallow water equations (SWE) on a set of common grids used in global circulation models (GCMs). Specifically, we study 1) the cubed-sphere (Sadourny 1972), 2) the icosahedral grid (Ico) (Sadourny *et al.* 1968), and 3) a type of reduced latitude-longitude (Lat-Lon) geometry (Phillips 1957). Because SWE capture many of the essential features of GCMs while eliminating the vertical structure of the atmosphere, the results from this study will be directly applicable to the fully three-dimensional model *NUMA*.

The geometry of the cubed-sphere and Lat-Lon grids can be advantageous for a finite difference based solver, and are generally usable by grid point methods such as finite and spectral element (FE, SE), DG, or finite volume (FV) methods. Furthermore, Lat-Lon is the standard discretization for GCMs based on spectral transform methods due to the fast Fourier transform operation along the longitude direction (Hogan *et al.* 1991). Icosahedral grids or, more generally, unstructured tri- and quad-based tessellations* of the sphere are geometrically flexible, but not all numerical methods are able to handle them. Recently, different grids to be used with finite volume discretization techniques have been analyzed in, e.g., Qaddouri *et al.* (2012) or Peixoto and Barros (2013). In the context of Galerkin methods, however, not much analysis has been conducted with respect to the solution dependence on these computational grids. Rather, given a specific grid, we are likely to find a model that is developed around it and is optimized to minimize the error in a specific configuration. In the case of the solution of shallow water problems, examples of this approach are the works by Taylor *et al.* (1997) (SE on cubed-sphere), Giraldo (2001) (SE on the quad-based icosahedral grid), Giraldo *et al.* (2002) (DG on a triangle-based icosahedral grid), or Nair *et al.* (2007) (DG on the cubed sphere). Recently, a comparison between dynamically adaptive and uniform meshes was performed by Müller *et al.* (2013) for triangle based discontinuous Galerkin methods. A grid comparison using spectral elements and/or finite volumes are found in St-Cyr *et al.* (2008) and Weller *et al.* (2009). However, the current work presents relevant differences in scope and goal with respect to these two articles. The differences can be listed as follows: St-Cyr et al. compare two different numerical methods that, by construction, are defined on two different grids. Their comparative analysis was made in terms of how a spectral element shallow water code and a finite volume code compare with each other. Their main concern was the verification of two codes when adaptive mesh refinement (AMR) was used with no emphasis, in that work, on the flexibility of either spectral elements or finite volumes with respect to the grid structure. On the other hand, Weller *et al.* (2009) show a finite volume analogous of what we partially show in this work using spectral elements. Since the main interest of our ongoing work in global atmospheric modeling is that of using Galerkin methods that should not, by design, be tied to any grid so that any optimized mesh generation tool could be used to build our grids, we found that we needed a comparison along the same lines of Weller et al., but taken from the point of view of continuous and discontinuous Galerkin methods.

Our study is performed by solving the two non-linear zonal flows proposed by Galewsky *et al.* (2004) first, followed by the test case 2 by Williamson *et al.* (1992) which admits the analytic solution of a steady state nonlinear geostrophic flow.

In the case of the Galewsky flow at low resolution, and because of the misalignment of the flows on the cubed-sphere and icosahedral grid, the solution diverges from the true solution in the case of (i) the equilibrium, and (ii) the

†Please ensure that you use the most up to date class file, available from the QJRMS Home Page at
http://onlinelibrary.wiley.com/journal/10.1002/(ISSN)1477-870X

*The keywords *grid, mesh*, and *tessellation* will be used interchangeably throughout the paper.

barotropic instability tests. As the resolution is increased, the effect of the irregular grid geometry is partially camouflaged and eventually disappears. In search of the coarsest allowable resolution to be used while still preserving accuracy, we add an artificial diffusion with constant coefficient $\nu = 1 \times 10^5\,\mathrm{m^2\,s^{-1}}$ as suggested by Galewsky *et al.* (2004). The viscous simulations are defined for CG only; no viscosity is used for DG.

Finally, to assess the ability of the model to handle conforming and non-conforming grids with refinement, we complete the study by building six statically adapted grids. We construct a fixed high-resolution grid core in the region where the zonal jet is most likely to develop, and coarsened the rest of the domain with a 1- and 2-level de-refinement approach to estimate the error when the total number of grid points is drastically reduced. The DG solution algorithm on the refined grids is based on the procedure by Kopera and Giraldo (2014) and references therein.

The paper is organized as follows. In Sec. 2, we report on the construction of high-order grids on the sphere. The model equations are described in Sec. 3 whereas the numerical method of solution is described in Sec. 4. We describe the tests and analyze the results in Sec. 5. Finally, we summarize our findings in Sec. 6.

2. High order grid generation on the sphere

Grid generation on the sphere is a relatively easy task. However, finding the grid that can suit different numerical methods is not. Because element-based Galerkin methods have the advantage of being flexible with respect to the grid, we analyze how different meshes on the sphere can affect the spectral element and discontinuous Galerkin solution of the shallow water equations.

A standard approach to high order grid generation is based on the construction of a linear grid first (i.e. a grid with straight edges whose extrema are the only points that lie on the geometry), and then populate it with the high order internal points. The population step is performed element-wise in the logical space obtained by a proper projection from the physical space. Once the higher order grid points have been built on the plane, a backward projection onto the physical geometry moves the new high order elements onto the sphere. This process is such that the high order elements approximate the surface faithfully. The projection from the sphere to the logical space may differ from grid to grid. The gnomonic projection by Ronchi *et al.* (1996) is used to build the high order grids. In what follows, we describe how the reduced Lat-Lon, cubed-sphere, and icosahedral grids are constructed.

2.1. *Reduced Lat-Lon grid (RLL)*

Since the effort of Phillips (1957) to reduce the singularity problem at the poles of a global latitude-longitude grid, different types of reduced Lat-Lon grids have been used. Partially based on the composite methods of Starius (1977) and Browning *et al.* (1989), Lanser *et al.* (2000) solved the shallow water equations on a Lat-Lon grid away from the poles combined with a stereographic grid at the poles. In this paper, we build and test a high order version of Lanser's grids. To build the RLL grid we use a multiblock approach (see, e.g., Thompson (1987)) that consists of building a set of independent, simply connected surface grids that are eventually patched together to form the global mesh. The main RLL region and the polar caps are the first blocks to be built. The interfaces between the RLL area and the polar patches are obtained by a transfinite interpolation (TFI, Gordon and Hall (1973); Eriksson (1984)). The way this is done will be described shortly. The main Lat-Lon region is composed of four faces obtained from the master face $\gamma_1 = [-\pi/4 \leq \lambda \leq \pi/4] \times [\varphi_{min} \leq \varphi \leq \varphi_{max}]$ and from its rotation with respect to the z-axis of the sphere. The variables λ and φ indicate the longitude and latitude, respectively. The RLL band in the northern and southern hemispheres is delimited by φ_{min} and φ_{max}. The rotation matrix from γ_1 to the three remaining faces $\gamma_2, \gamma_3, \gamma_4$ is obtained by the combined effect of a translation on the xy-plane and a rotation around the z-axis; this transformation is given by

$$[\mathrm{T}] = \begin{bmatrix} 1 & 0 & 0 & 0 \\ 0 & 1 & 0 & 0 \\ 0 & 0 & 1 & 0 \\ l & m & n & 1 \end{bmatrix} \begin{bmatrix} \cos(\lambda_{rot}) & \sin(\lambda_{rot}) & 0 & 0 \\ -\sin(\lambda_{rot}) & \cos(\lambda_{rot}) & 0 & 0 \\ 0 & 0 & 1 & 0 \\ 0 & 0 & 0 & 1 \end{bmatrix}.$$

The first matrix produces a translation $[l\, m\, n] = [-1\, -1\, -1]$ along (x, y, z) and is followed by the rotations $\lambda_{rot,i=2,3,4} = (\pi/2, \pi, 3\pi/2)$ given by the action of the second matrix. The coordinates on each rotated planar face are simply a function of $(x, y, z)_{\gamma_1}$ and are computed as

$$[x\ y\ z\ 1]_{\gamma_i} = [x\ y\ z\ 1]_{\gamma_1}[T], \quad i = 2, 3, 4. \tag{1}$$

Once rotated, each gridded face is projected onto the sphere. The polar caps are built in the same way, except that the starting point is the square region $\gamma_{polar} = [-\pi/4 \leq \lambda \leq \pi/4] \times [-\pi/4 \leq \varphi \leq \pi/4]$. At this point we have a linear grid made of 6 disjoint regular patches. The top view of this is shown in Fig. 1. Eight new surfaces must now be built to fill the un-gridded gaps.

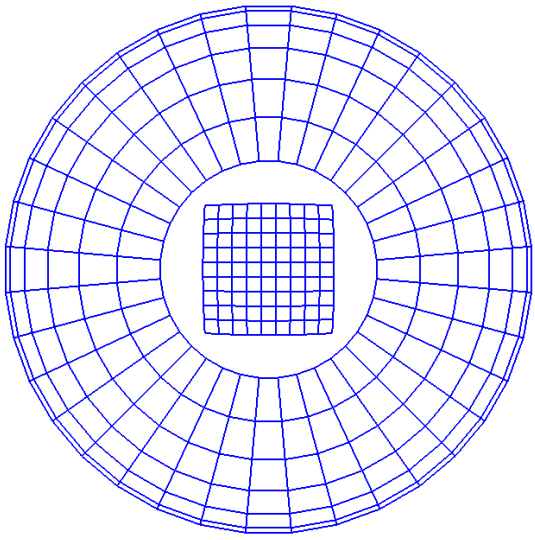

Figure 1. Linear grid. Top $x - y$ view of the disjoint lateral Lat-Lon and top patches in the multi-block RLL grid. TFI is used to connect them together through an interface surface grid.

To build each interface surface by TFI we need information from its four boundary edges. With reference to the schematic of Fig. 2, the region delimited by edges $1, 2, 3, 4$ is built in two steps: *(a)* given the (λ, φ) coordinates of the corner points 1-2-3-4, build edges 3 and 4 and subdivide them into $N_{e_{lat,int}}$ 1D linear elements, where $N_{e_{lat,int}}$ is the user-defined number of elements along the latitude direction in the interface region; *(b)* compute the grid points in the interior of the patch using the planar and linear transfinite interpolation defined by the Boolean sum

$$\mathbf{X}(\hat{\xi}, \hat{\eta}) = \mathbf{U} + \mathbf{V} - \mathbf{U} \otimes \mathbf{V}, \tag{2}$$

where, given the arrays $\hat{\xi} = [0, \ldots, 1]$ and $\hat{\eta} = [0, \ldots, 1]$ in computational space along the local $(\hat{u}, \hat{v})$ directions, the univariate interpolations and tensor products $(\otimes)$ are computed as

$$\begin{aligned} \mathbf{U}(\hat{\xi}, \hat{\eta}) &= (1 - \hat{\xi})\mathbf{X}(0, \hat{\eta}) + \hat{\xi}\mathbf{X}(1, \hat{\eta}) \\ \mathbf{V}(\hat{\xi}, \hat{\eta}) &= (1 - \hat{\eta})\mathbf{X}(\hat{\xi}, 0) + \hat{\eta}\mathbf{X}(\hat{\xi}, 1) \\ \mathbf{U} \otimes \mathbf{V}(\hat{\xi}, \hat{\eta}) &= (1 - \hat{\xi})(1 - \hat{\eta})\mathbf{X}(0, 0) + (1 - \hat{\xi})\hat{\eta}\mathbf{X}(0, 1) \\ &\quad -(1 - \hat{\eta})\hat{\xi}\mathbf{X}(1, 0) - \hat{\xi}\hat{\eta}\mathbf{X}(1, 1). \end{aligned} \tag{3}$$

In Equations (2), $\mathbf{X}$ is the array of the (λ, φ) coordinates of the grid points in the interior of the surface, given the known values of the surface boundary edges stored in $\mathbf{X}(0, \hat{\eta}), \mathbf{X}(1, \hat{\eta}), \mathbf{X}(\hat{\xi}, 0), \mathbf{X}(\hat{\xi}, 1)$, and corners $\mathbf{X}(0, 0), \mathbf{X}(1, 1), \mathbf{X}(1, 0), \mathbf{X}(0, 1)$.

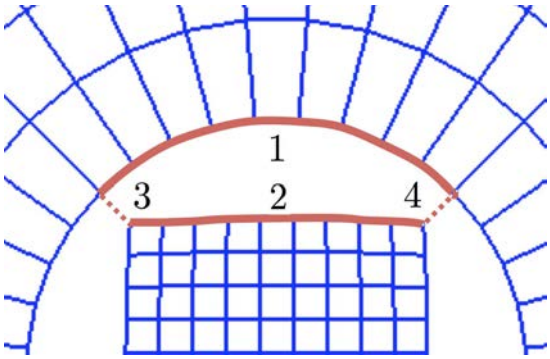

Figure 2. Detail of one interface patch in the northern hemisphere.

The high-order Legendre-Gauss-Lobatto (LGL) points are added to the linear grid by projecting the linear elements onto the auxiliary gnomonic space (on the plane), and back-projecting the new high order quads onto the sphere. The total number of elements N_e and grid points N_p of the high order conforming grid are given by:

$$
\begin{aligned}
N_e = & \\
& 4N_{e_{lon}}N_{e_{lat}} && \text{Lateral Lat-Lon} \\
& +2N_{e_{lon}}N_{e_{lon}} && \text{Polar caps} \\
& +8N_{e_{lon}}N_{e_{lat,int}} && \text{Transition zone,}
\end{aligned} \tag{4}
$$

and

$$
\begin{aligned}
N_p = & \\
& 4N_{e_{lon}}N(N_{e_{lat}}N+1) && \text{Lateral} \\
& +2(N_{e_{lon}}N+1)(N_{e_{lon}}N+1) && \text{Polar} \\
& +2(4N_{e_{lon}}N(N_{e_{lat,int}}N+1)-8N_{e_{lon}}N) && \text{Transition.}
\end{aligned} \tag{5}
$$

In (4) and (5), $N_{e_{lon}}$ is the number of elements of order N along the longitude direction of one face in the main Lat-Lon band that, by construction, coincides with the number of longitude elements in the interface and polar regions. $N_{e_{lat}}$ and $N_{e_{lat,int}}$ are, respectively, the number of latitude elements of the Lat-Lon region and of the interface patches. The number of latitude elements in the polar caps is also given by $N_{e_{lon}}$. Fig. 3 shows an example of a high-order conforming RLL tessellation.

We want to point out that this procedure to build the multi-block spherical grid is not unique and can be certainly optimized to give the best distribution of the high order grid points. The goal of our study is not to propose the most optimized grid generators but rather to analyze how an element-based Galerkin model handles arbitrarily generated grids.

2.2. *Cubed-sphere*

The cubed sphere (see, e.g. Ronchi *et al.* (1996); Taylor *et al.* (1997, 2013)) is derived from the projection of a cube onto the sphere. As such, it consists of 6 faces that are then subdivided into as many elements as necessary. Like RLL, we built this grid in a multi-block fashion by going through the same steps described above. The fundamental difference is that the cubed-sphere grid (also referred to as Hex in the Figures and Tables throughout the paper) has only 6 faces and they are all equal. An example is shown in Fig. 4. The internal

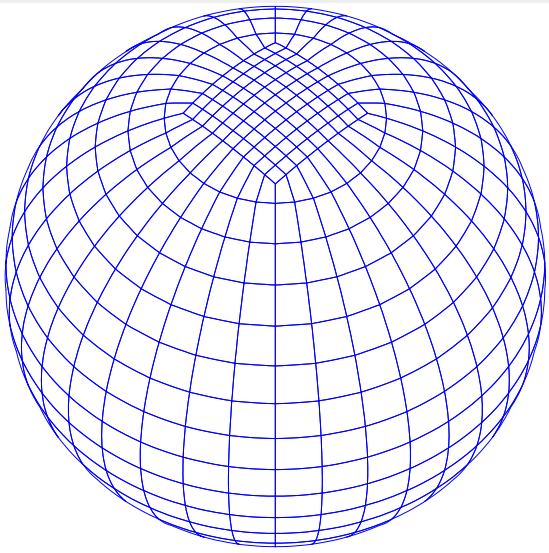

Figure 3. Conforming RLL grid.

LGL points are omitted for the sake of a clearer plot. By construction, the elements that are farthest from the center of each face are smaller than those at the face center; in addition, their distorted shape prove to be a concern when the resolution is not sufficiently high. We will discuss this issue shortly.

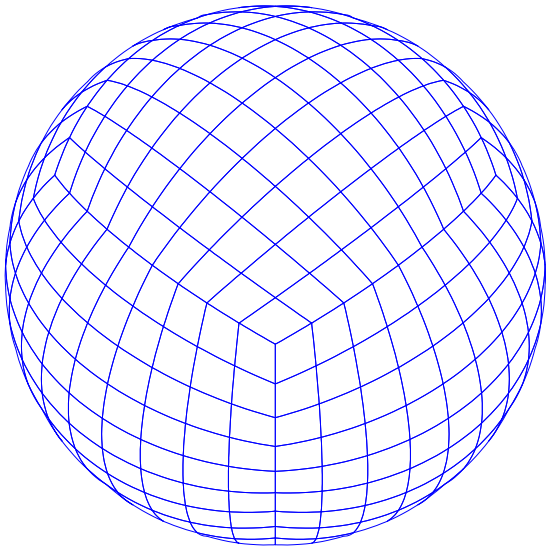

Figure 4. Conforming Hex grid.

2.3. *Quad-based icosahedral grid*

The quad-based icosahedral grid of order N is derived from an initial icosahedron of 20 triangles. For better properties of the high order grid, every triangle is mapped onto a gnomonic space by the transformation formulas (Giraldo (2001))

$$x = r\tan\lambda', \tag{6a}$$

$$y = r \tan\varphi' \sec\lambda', \tag{6b}$$

where r is the radius of the sphere and, given the centroids (λ_c, φ_c) of each triangle, we define

$$\lambda' = \text{atan}\left[\frac{\cos\varphi \sin(\lambda - \lambda_c)}{\cos\varphi_c \sin\varphi + \cos\varphi_c \cos\varphi \cos(\lambda - \lambda_c)}\right], \tag{7a}$$

$$\varphi' = \text{asin}\left[\cos\varphi_c \sin\varphi - \sin\varphi_c \cos\varphi \cos(\lambda - \lambda_c)\right]. \tag{7b}$$

After mapping, the triangles are subdivided into smaller ones by a Lagrange polynomial of order n_I.

The number of quadrilateral elements and grid points of the final grid are then given by

$$N_p = 6(N_p^T - 2)N^2 + 2$$
$$N_e = 6(N_p^T - 2)$$

where the number of points N_p^T of the original triangular grid can be found in Giraldo (2001).

Fig. 5 shows the 8^{th} order icosahedral grid. As for the previous cases, the elements are curved and lie on the spherical surface.

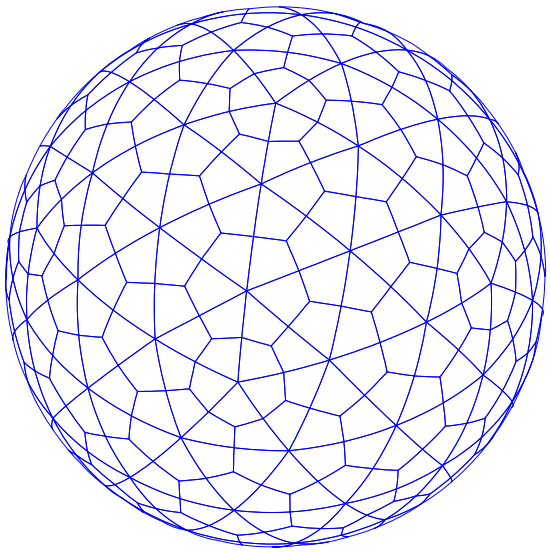

Figure 5. Conforming Ico grid.

3. Shallow water equations on the sphere

3.1. *Equations of motion*

Under the assumption of a shallow depth, the motion of an incompressible fluid may be described by the non-linear shallow water equations. The shallow water assumption holds as long as the characteristic horizontal extension of the fluid is much larger than its depth. The vector representation of the shallow-water equations in the Cartesian coordinates $\mathbf{x} = (x, y, z)$ is given, in flux form, by

$$\frac{\partial\phi}{\partial t} + \nabla\cdot(\phi\mathbf{u}) = 0 \tag{8a}$$

$$\frac{\partial\phi\mathbf{u}}{\partial t} + \nabla\cdot(\phi\mathbf{u}\otimes\mathbf{u}) = -\phi\nabla\phi - f(\mathbf{x}\times\phi\mathbf{u}) + \mu\mathbf{x} + \delta\nu\nabla^2(\phi\mathbf{u}) \tag{8b}$$

where $\phi = gh$ is the geopotential height (g and h are the modulus of the acceleration of gravity and the vertical height of the fluid), $\nu\nabla^2$ is the artificial viscosity term of viscous coefficient $\nu = 1\times10^5\,\text{m}^2\,\text{s}^{-1}$ that is de-activated by the switch $\delta = 0$, $\mathbf{u} = (u, v, w)^\mathcal{T}$ is the velocity vector, $\nabla = (\partial_x, \partial_y, \partial_z)^\mathcal{T}$, and $f = 2\omega z/r^2$ is the Coriolis parameter with Earth's angular velocity $\omega = 7.292\times10^{-5}\,\text{s}^{-1}$ and mean radius $r = 6.37122\times10^6$m. For the fluid particles to remain on the spherical surface defined in 3D Cartesian space, the normal component of the velocity field with respect to the sphere is removed by the term $\mu\mathbf{x}$ in the momentum equation, where μ is the Lagrange multiplier that serves this purpose. The construction of the Lagrange multiplier is described in Sec. 3.2.

3.2. *Forcing the fluid onto the sphere by a Lagrange multiplier*

We use the approach of Coté (1988). Specifically, at the end of every time step $n+1$, the momentum of the flow must be corrected for the particles to remain on the sphere. If c and u denote the *c*onstrained and *u*nconstrained values of $\phi\mathbf{u}$, the new momentum is corrected according to

$$(\phi\mathbf{u})_c^{n+1} = (\phi\mathbf{u})_u^{n+1} + \mu\mathbf{x}. \tag{9}$$

For the fluid to remain on the sphere, the condition $\mathbf{u} \cdot \mathbf{x} = 0$ must hold (i.e., the velocity field and the position vector must be orthogonal), hence implying that $\phi \mathbf{u}_c \cdot \mathbf{x} = 0$ in Equation (9). For this to be true, the value of the multiplier is found to be $\mu = -\phi \mathbf{u}_u^{n+1} \cdot \mathbf{x}/r^2$. Substituting this into Eq. (9) yields

$$(\phi \mathbf{u})_c^{n+1} = \mathcal{P} \, (\phi \mathbf{u})_u^{n+1}, \tag{10}$$

where

$$\mathcal{P} = \mathbf{I} - \frac{\mathbf{x}\mathbf{x}^{\mathcal{T}}}{r^2} \tag{11}$$

is an orthogonal projector. $\mathcal{T}$ indicates the transpose operator.

The Galerkin discretization of (8) is described in the next section.

4. Numerical method

4.1. Spectral element and discontinuous Galerkin approximations

To solve the shallow water equations by element-based Galerkin methods on a domain Ω, we proceed by defining the weak form of (8) that we first write in compact form as

$$\frac{\partial \mathbf{q}}{\partial t} + \nabla \cdot \mathbf{F}(\mathbf{q}) = \mathbf{S}(\mathbf{q}), \tag{12}$$

where $\mathbf{q} = [\phi, \phi \mathbf{u}]^{\mathcal{T}}$ is the array of the solution variables, and $\mathbf{F}$ and $\mathbf{S}$ are the flux and source terms that can be easily identified in the equations (8) above. Given a basis function ψ that belongs to the Sobolev space H^1 in the case of spectral elements, and to L^2 in the case of DG, the weak form of (12) is given by the integral

$$\int_\Omega \psi \left[\frac{\partial \mathbf{q}}{\partial t} + \nabla \cdot \mathbf{F}(\mathbf{q}) - \mathbf{S}(\mathbf{q}) \right] d\Omega = 0, \tag{13}$$

that, after integration by parts of the flux, becomes

$$\int_\Omega \psi \frac{\partial \mathbf{q}}{\partial t} \, d\Omega - \int_\Omega \nabla \psi \cdot \mathbf{F}(\mathbf{q}) \, d\Omega - \int_\Omega \psi \mathbf{S}(\mathbf{q}) \, d\Omega + \int_\Gamma \psi \mathbf{n} \cdot \check{\mathbf{F}}(\mathbf{q}) \, d\Gamma = 0, \tag{14}$$

where $\check{\mathbf{F}}(\mathbf{q})$ indicates the numerical flux of the advection and diffusion terms across the element boundary Γ of unit outward normal $\mathbf{n}$. In the case of spectral elements, where the basis functions are continuous across neighboring elements, and given that the problem is solved on a closed manifold, the boundary integral $\int_\Gamma$ vanishes. On the other hand, in the case of the DG method, the boundary integral remains because of the non-zero inter-element fluxes. Furthermore, the surface integrals for DG are defined element-wise over Ω_e rather than globally over Ω. This makes Equations (13) and (14) a system of N_e equations that are coupled via the flux of Equation (14). Both options are available within the same code used for this study and both methods share most of the numerical machinery.

The integrals above are solved element-wise on the discrete polyhedral approximation Ω^h. The discrete domain Ω^h is defined by the union of N_e non-overlapping quadrilateral elements Ω_e^h. For every element we define a bijective transformation $\mathcal{F}_{\Omega_e^h} : (x, y, z) \to (\xi, \eta, \zeta)$ that maps the physical coordinate system, (x, y, z) to the reference system (ξ, η, ζ) and is such that the reference element $\hat{\Omega}_e^h(\xi, \eta) = [-1, 1] \times [-1, 1]$ lies on the spherical surface. ζ is thus the spherical radius whose discrete values identify a spherical shell (e.g. $\zeta = 1$ is the sphere of unit radius.) The Jacobian matrix of the transformation has components $J^i = \partial_\xi \mathcal{F}^i$ and determinant $|\mathbf{J}| = \partial_\zeta \mathbf{x} \cdot \mathbf{G}$, where $\mathbf{G} = \partial_\xi \mathbf{x} \times \partial_\eta \mathbf{x}$ is the surface conforming component of the transformation (Song and Wolf 1999; Giraldo 2001).

Given the definition of the reference element, the element-wise solution can be approximated by the expansion

$$q_N(\mathbf{x}, t)|_{\Omega_e} = \sum_{k=1}^{(N+1)^2} \psi_k(\mathcal{F}_{\Omega_e}^{-1}(\mathbf{x})) \, q_N(\mathbf{x}_k, t), \; e = 1, \ldots, N_e \tag{15}$$

where $(N+1)^2$ is the number of collocation points within the element of order N, and ψ_k are the interpolation polynomials evaluated at point k. The basis functions ψ_k are constructed as the tensor product of the one-dimensional functions $h_i(\xi(\mathbf{x}))$ and $h_j(\eta(\mathbf{x}))$ as:

$$\psi_k = h_i(\xi(\mathbf{x})) \otimes h_j(\eta(\mathbf{x})),$$

$\forall i,j = 0,...,N$. $h_i(\xi(\mathbf{x}))$ and $h_j(\eta(\mathbf{x}))$ are the basis functions associated with the $N+1$ LGL points ξ_i and η_j, respectively, given by the roots of

$$(1-\xi^2)P_N^{'}(\xi) = 0,$$

where $P_N'(\xi)$ is the derivative of the N^{th}-order Legendre polynomial. Given these definitions, the one-dimensional Lagrange polynomials $h_i(\xi)$ are

$$h_i(\xi) = -\frac{1}{N(N+1)}\frac{(1-\xi^2)P_N'(\xi)}{(\xi-\xi_i)P_N(\xi_i)}.$$

The functions $h_j(\eta)$ are computed in the same way.

The same expansion above is used to construct the derivatives. We write:

$$\begin{aligned}\frac{\partial q_N(\mathbf{x},t)}{\partial t}|_{\Omega_e} &= \sum_{k=1}^{(N+1)^2}\psi_k(\mathcal{F}_{\Omega_e}^{-1}(\mathbf{x}))\frac{\partial q_N(\mathbf{x}_k,t)}{\partial t},\\ \frac{\partial q_N(\mathbf{x},t)}{\partial \mathbf{x}}|_{\Omega_e} &= \sum_{k=1}^{(N+1)^2}\frac{\partial\psi_k(\mathcal{F}_{\Omega_e}^{-1}(\mathbf{x}))}{\partial \mathbf{x}}q_N(\mathbf{x}_k,t). \quad (16)\end{aligned}$$

The integrals are computed by numerical quadrature on the reference element as follows:

$$\int_{\Omega_e^h}\mathbf{q}(\mathbf{x},t)\mathrm{d}\mathbf{x} = \int_{\hat{\Omega}_e^h}\mathbf{q}(\xi,t)|\mathbf{J}(\xi)|\mathrm{d}\xi \approx \sum_{i=1}^{N+1}\sum_{j=1}^{N+1}q(\xi_i,\eta_j,t)|\mathbf{J}(\xi_i,\eta_j)|\omega_i^\xi\omega_j^\eta, \quad (17)$$

where ω_i, ω_j are the Gaussian quadrature weights. In the case of spectral elements, the substitution of the expansions (15,16) into the weak form (14) yields the semi-discrete (in space) matrix problem

$$\frac{\partial \mathbf{q}}{\partial t} = \widehat{\mathbf{D}}^{\mathcal{T}}\mathbf{F}(\mathbf{q}) + \mathbf{S}(\mathbf{q}) \quad (18)$$

where, for the global mass and differentiation matrices, $\mathbf{M}$ and $\mathbf{D}$, we have that $\widehat{\mathbf{D}} = \mathbf{M}^{-1}\mathbf{D}$. The global matrices are obtained from their local counterparts, $\mathbf{M}^e$ and $\mathbf{D}^e$, by means of the direct stiffness summation operation that maps the local degrees of freedom of an element Ω_e^h to the corresponding global degrees of freedom in Ω^h, and adds the element values in the global system. By construction, $\mathbf{M}$ is diagonal (assuming inexact integration), with an obvious advantage if explicit time integration is used.

Concerning the discontinuous Galerkin approximation, the problem at hand is solved only locally, and unlike the case of spectral elements, the flux integral in Equation (14) must be discretized as well. The element-wise counterpart of the matrix problem (18) is then written as:

$$\frac{\partial \mathbf{q}^e}{\partial t} = -(\widehat{\mathbf{M}}^{s,e})^{\mathcal{T}}\breve{\mathbf{F}}(\mathbf{q}^e) + (\widehat{\mathbf{D}}^e)^{\mathcal{T}}\mathbf{F}(\mathbf{q}^e) + \mathbf{S}(\mathbf{q}^e), \quad (19)$$

where we obtain $\widehat{\mathbf{M}}^{s,e} = (\mathbf{M}^e)^{-1}\mathbf{M}^{s,e}$ from the element boundary matrix, $\mathbf{M}^{s,e}$, and the element mass matrix, $\mathbf{M}^e$. Out of various possible choices for the definition of the numerical flux $\breve{\mathbf{F}}(\mathbf{q})$ in Equation (19), we selected the Rusanov flux that, for the inviscid part of the flux, is

$$\breve{\mathbf{F}}(\mathbf{q}) = \frac{1}{2}\left[\mathbf{F}_N(\mathbf{q}_N^L) + \mathbf{F}_N(\mathbf{q}_N^R) - |\lambda|(\mathbf{q}_\mathbf{N}^\mathbf{R} - \mathbf{q}_N^L)\mathbf{n}\right], \quad (20)$$

where $|\lambda| = |\mathbf{n}\cdot\mathbf{u}| + \sqrt{\phi}$ is the maximum wave speed of the shallow water equations. By identifying an intrinsic tangential direction in each inter-element boundary edge, $\mathbf{q}_N^L$ and $\mathbf{q}_N^R$ denote the solution in the left (L) and right (R) elements, respectively. For a detailed description of the DG algorithm that is used for this study, the reader is referred to Kopera and Giraldo (2014).

4.2. Time integration

The solution of the systems of ordinary differential equations (18,19) is advanced in time by a third-order strong stability preserving Runge-Kutta method (SSP-RK3) (Cockburn and Shu 2001; Spiteri and Ruuth 2002) that yields the solution at time-step $n+1$ as

$$\mathbf{q}^k = \alpha_0^k\mathbf{q}^n + \alpha_1^k\mathbf{q}^{k-1} + \beta^k\Delta t\, R(\mathbf{q}^{k-1}), \text{for } k = 1,\dots,K,$$

where $R(\mathbf{q})$ indicates the right-hand sides of equations (18,19), K is the number of stages of the RK method, and $\mathbf{q}^0 = \mathbf{q}^n, \mathbf{q}^K = \mathbf{q}^{n+1}$. All the computations are executed with a maximum Courant-Friedrichs-Lewy number (CFL, Courant *et al.* (1967)) approximately 0.5. This value ensures

the stability of the scheme given that the time step Δt is such that

$$\Delta t \leq CFL \min_{\mathbf{x}\in\mathbf{\Omega^h}} [|\mathbf{u}\cdot\boldsymbol{\chi}| + \phi\sqrt{\boldsymbol{\chi}\cdot\boldsymbol{\chi}}]^{-1}.$$

The $CFL \propto \Delta t|\mathbf{u}|/\Delta|\mathbf{x}|_{min}$, where $\Delta|\mathbf{x}|_{min}$ gets smaller with the order N.

The local grid distortion, $\boldsymbol{\chi}$, is defined as the vector

$$\boldsymbol{\chi} = \left(\frac{|\xi_x|}{\Delta\xi} + \frac{|\eta_x|}{\Delta\eta}, \frac{|\xi_y|}{\Delta\xi} + \frac{|\eta_y|}{\Delta\eta}, \frac{|\xi_z|}{\Delta\xi} + \frac{|\eta_z|}{\Delta\eta}\right)$$

where $\xi_{x,y,z}$ and $\eta_{x,y,z}$ are the metric terms and $\Delta\xi, \Delta\eta$ are the local average grid sizes across the surface.

In the absence of dissipation (e.g., artificial diffusion), the high order numerical solution of advective problems may be characterized by spurious high frequency modes. To preserve full stability, along with respecting the CFL condition we applied the standard spatial Boyd-Vandeven filter (Boyd 1996) at every time step. The filter constant is chosen to reduce by 5% the highest modes only.

5. Tests

To evaluate the behavior of the solution on the three grid families, we first solve the nonlinear zonal dynamics test by Galewsky *et al.* (2004) whose exact analytic solution is unknown, and follow with the steady state nonlinear geostrophic flow by Williamson *et al.* (1992) that, on the contrary, admits an analytic solution. The tests are run at different resolutions using elements of order 8; based on the analysis by Gaberšek *et al.* (2012), 8 is the order that we are likely to use when running simulations with NUMA.

The test by Galewsky *et al.* (2004) consists of (i) an unperturbed mid-latitude zonal jet on top of a geostrophically balanced geopotential height, and of (ii) its perturbed counterpart where the perturbation is triggered by a bump in the geopotential. In either case, the initial zonal velocity and height are a function of the latitude φ (measured in radians unless otherwise specified) as

$$u(\varphi) = \begin{cases} 0 & \text{if } \varphi \leq \varphi_0 \text{ or } \varphi \geq \varphi_1 \\ \frac{u_{\max}}{e_n}\exp\left[\frac{1}{(\varphi-\varphi_0)(\varphi-\varphi_1)}\right] & \text{if } \varphi_0 < \varphi < \varphi_1, \end{cases} \quad (21)$$

where $u_{max} = 80\,\mathrm{m\,s^{-1}}$ is the maximum zonal velocity and $(\varphi_0, \varphi_1) = (\pi/7, \pi/2 - \varphi_0)$ are the lowest and highest latitudes that delimit the jet. At the jet mid-point, where $\varphi = \pi/4$, the non-dimensional parameter $e_n = \exp[-4/(\varphi_1 - \varphi_0)^2]$ normalizes the jet magnitude to $u_{\max}$. From the initial zonal flow given by (21), the height ϕ is found by solving

$$g\phi(\varphi) = g\phi_0 - \int^{\varphi} ru(\varphi')\left[f + u(\varphi')\frac{\tan(\varphi')}{r}\right]d\varphi', \quad (22)$$

where the integral on the right-hand side is computed by numerical quadrature. As in the reference, φ_0 is chosen to give a global mean layer depth of 10 km. The height perturbation of test (ii) is the bump whose shape is given by

$$\phi'(\lambda,\varphi) = \hat{\phi}\cos(\varphi)\exp[-\lambda^2/\alpha^2]\exp[-(\varphi_2-\varphi_1)^2/\beta^2] \quad \text{for } -\pi < \lambda < \pi, \quad (23)$$

where λ is the longitude, $\hat{\phi} = 120\,\mathrm{m}$, $\varphi_2 = \pi/4$, $\alpha = 1/3$ and $\beta = 1/15$. The definition of this bump is such that the perturbation is forced to zero at the poles.

The flows in (i) and (ii) are simulated along a time span of 144 hours. In the absence of any perturbation, the balanced field and zonal flow are expected to maintain their initial state indefinitely. The analytical initial field is used to compute the L_2 error norms of the numerical solutions as time evolves.

Although its solution seems trivial, this test is especially demanding for a shallow water model because of the large sensitivity of the solution to the grid resolution and geometry.

Unlike other tests that may be more forgiving in this respect, when the grid is not sufficiently fine, grid related oscillations may spoil the equilibrium with devastating consequences. This is clearly visible in Fig. 6, where the initially unperturbed and balanced zonal flow completely loses its initial state when the test is executed on the low resolution cubed-sphere and icosahedral grids. All the runs are executed at the equivalent resolutions $\Delta\lambda \approx \Delta\varphi = \{0.625^\circ, 1.25^\circ, 2.5^\circ, 5.0^\circ\}$ and for a varying number of grid points $N_p = \{12000, 25000, 50000, 100000\}$. The reason for the two sets of runs will be clarified in *Remark 1.*

Below, the keywords *Equilibrium* and *Perturbed jet* are used to identify, respectively, problems (i) and (ii).

Remark 1: equivalent resolutions A few words are in order regarding the concept of *equivalent resolution* when grids of very different geometries are compared. In the case of spectral elements that rely on LGL nodes, the distance between two consecutive grid points changes within the same element. Because of this, the equivalent angular resolution along a latitude circle subdivided into $N_{e,\lambda}$ elements of order N is $2\pi/(N_{e,\lambda}N)$. Given this definition, we add that two resolutions are approximately equivalent when, within the region of major interest (e.g., where the dynamics is most likely to develop from a certain initial state), the size of the angular resolution of two different grids are comparable. In other words, when we say that the resolution is, e.g., $\Delta\lambda = 0.625^\circ$, it means that the mean angular distance between two meridians in the proximity of the jet measures 0.625°. This definition makes the measurement on the icosahedral grid not straightforward because of the irregular orientation of the elements. To obviate this problem, the error norms in the analysis below are also compared with respect to the total number of grid points.

5.1. *Equilibrium*

Fig. 6 shows the vorticity field after 6 days for the unperturbed (Equilibrium) jet problem on the three different conforming grid types (rows) and $N_p = \{25000, 50000, 100000\}$ grid points. For two out of the three grid geometries, the effect of the misalignment is still important for as many as 25000 grid points, which approximately corresponds to an equivalent resolution $\Delta\lambda = \Delta\varphi = 1^\circ$ on the cubed-sphere. The solution on the RLL grid can maintain the jet with approximately 80% fewer grid points than the cubed-sphere grid and 50% fewer than the icosahedral grid. This is not reason enough to draw conclusions on the possible superiority of one grid with respect to the others; rather, it should only suggest that, unless a sufficiently high resolution is used with grids that are not aligned with the characteristic flow (which is likely to be the case in realistic simulations), we should not trust the solution with high fidelity.

In Figs. 7 and 8 we plot the normalized L_2 error norms of the geopotential height and zonal velocity against the number of grid points and, respectively, the equivalent resolution $(\Delta\lambda, \Delta\varphi)$ (see the tabulated values of all the errors plotted in the paper, in the Appendix). These errors are computed using spectral elements on conforming grids. Let us focus on the curves with continuous lines as they trace the error on the uniform conforming grids. The conclusions drawn from the vorticity contours of Fig. 6 are confirmed by these error estimates. Furthermore, from Fig. 8 it is interesting to see that the L_2 error of the solution on the cubed-sphere reaches its peak value at $\Delta\varphi = \Delta\lambda \approx 1.25^\circ$. This leaves very little room for resolution options when the cubed-sphere is used without viscosity at low resolution.

The results reported so far were obtained using CG on conforming grids. However, we also ran the same tests using DG on every grid. As expected, the errors are practically identical to those obtained by CG; the solution accuracy for CG and DG should be identical because the solution is relatively smooth (differences should only emerge between the two methods in the presence of discontinuities). For comparison, we report the values of the CG and DG normalized error norms in Tables 3 and 5 in the Appendix. We will show DG results on non-conforming grids with static refinement in Sec. 5.3.

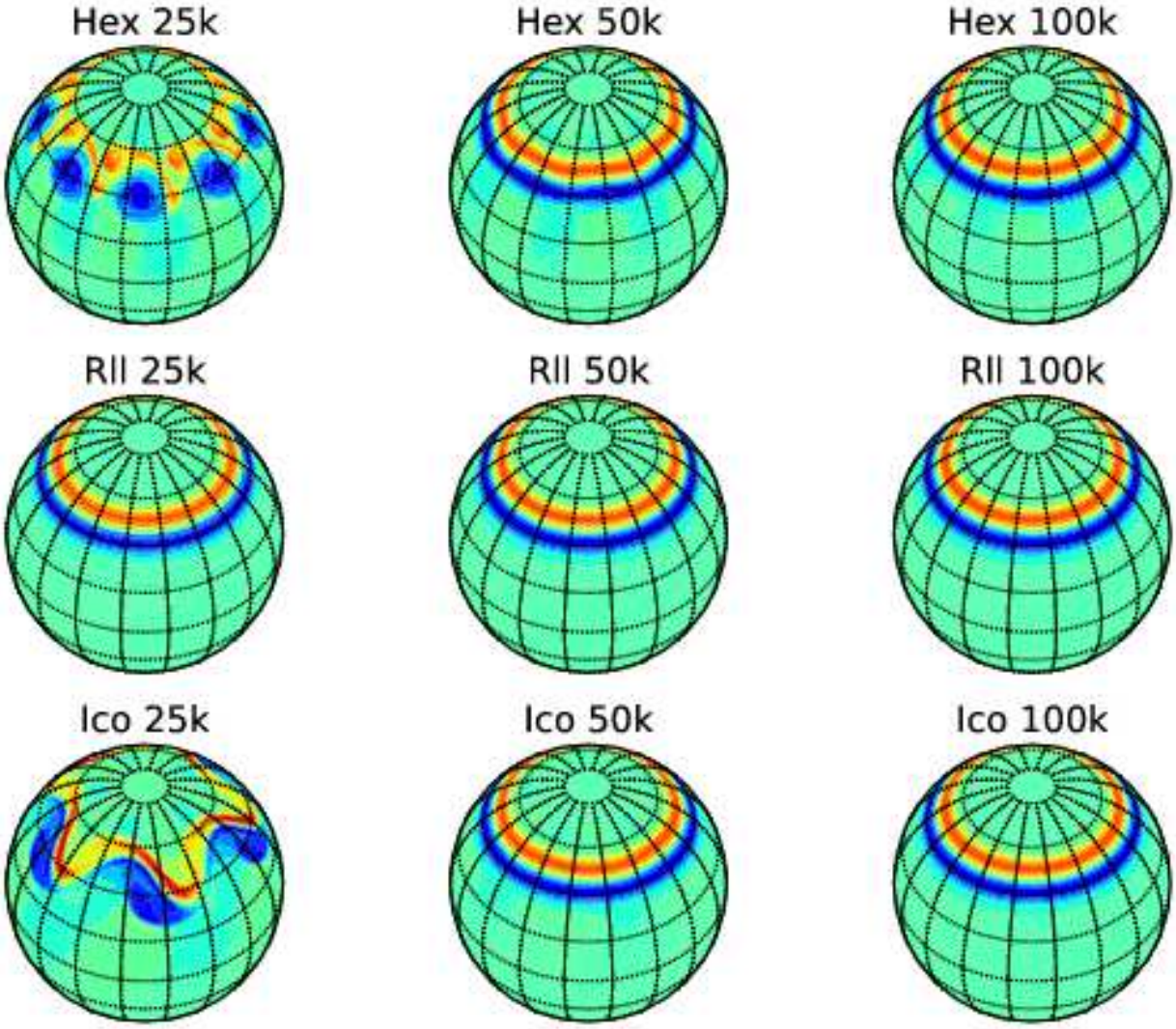

Figure 6. *Equilibrium*, inviscid CG solution: vorticity field (s^{-1}) after 6 days. The solutions on the cubed-sphere (Hex, top row), on the RLL (middle), and on the icosahedral grids (bottom row) are plotted from left to right using 25000, 50000, and 100000 grid points. The color scale ranges between -12×10^{-5} s^{-1} (dark blue) and 16×10^{-5} s^{-1}.

In Fig. 9 we plot the time evolution of $\|\phi\|_{L_2}$ during 6 days for 100000 point grids. After the gravity wave adjustment during the first 6 hours (see Galewsky *et al.* (2004)), the regularity of the grid geometry still plays an important role in the evolution of the error even at a resolution that, in global mode, is typically considered fairly high in an operational setting.

So far, the viscous term in the equations has been ignored (i.e. $\delta = 0$). In the quest for diminishing the negative effects of the low resolution on certain grids, we turned viscosity on and recomputed the normalized L_2 error norms that we report in Table 1. We compare these errors against the inviscid estimates using 12000 and 25000 grid points and point out the instances when artificial viscosity is either beneficial or harmful to the error measure. To interpret these values, we need to take a parallel look at the contour plots of Fig. 10. In the case of RLL, where the grid is aligned with the characteristic flow, it was shown above that the resolution does not significantly affect the solution. The opposite, however, occurs in the case of the other two grids. Not surprising, by adding viscosity, what was a bad inviscid solution seems to improve; in contrast, the solution that was well behaved in the inviscid case has deteriorated. This behavior is expected for two main reasons: (1) the viscous and inviscid equations are, mathematically, not the same set of equations, and physically represent two different dynamics; (2) viscosity is so large that it is damping all of the modes triggered by the grid on the one hand but, in the same way, damps the solution also where it should not. A thorough analysis of the diffusion mechanisms that are currently used

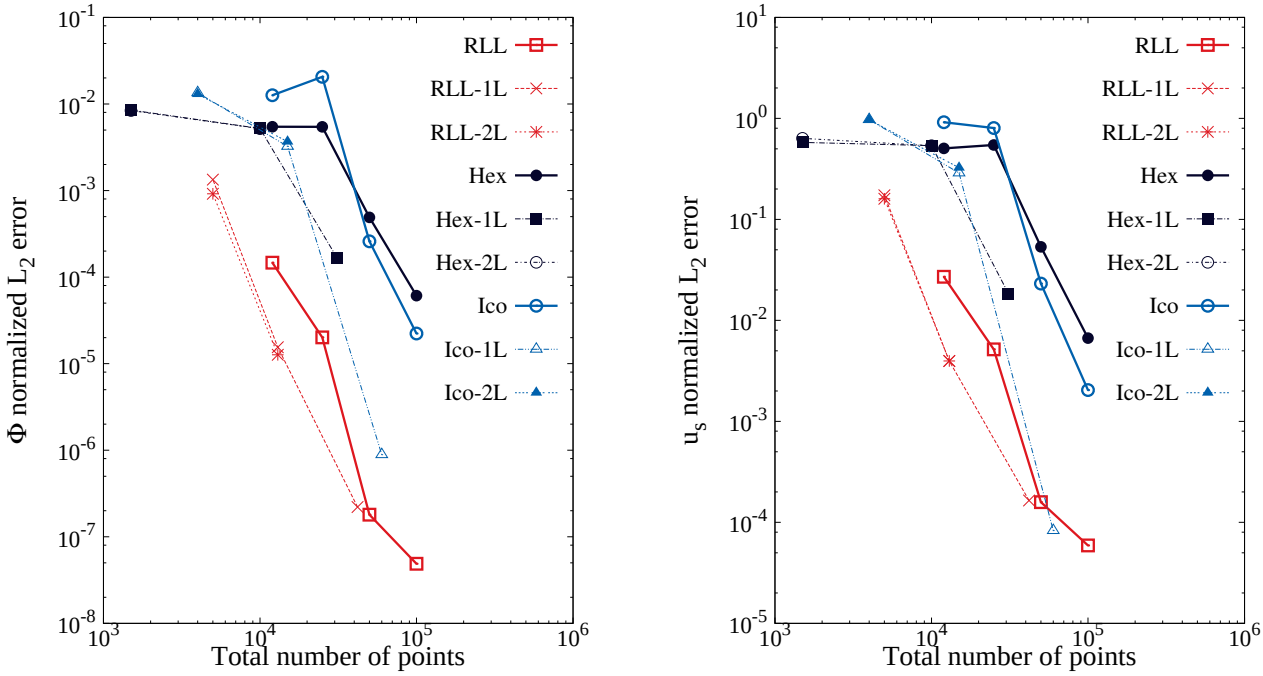

Figure 7. *Equilibrium* at day 6, inviscid: Normalized L_2 error norm of ϕ (left) and u_s (right) against the number of grid points. The error is computed with respect to the initial condition of the balanced problem on every grid. In the legend, the symbols *1L* and *2L* indicate that the solution is computed on a non-conforming grid with 1 or 2 levels of refinement. In these two cases, the solution is computed using DG, otherwise, CG is used instead. See tabulated values in the Appendix.

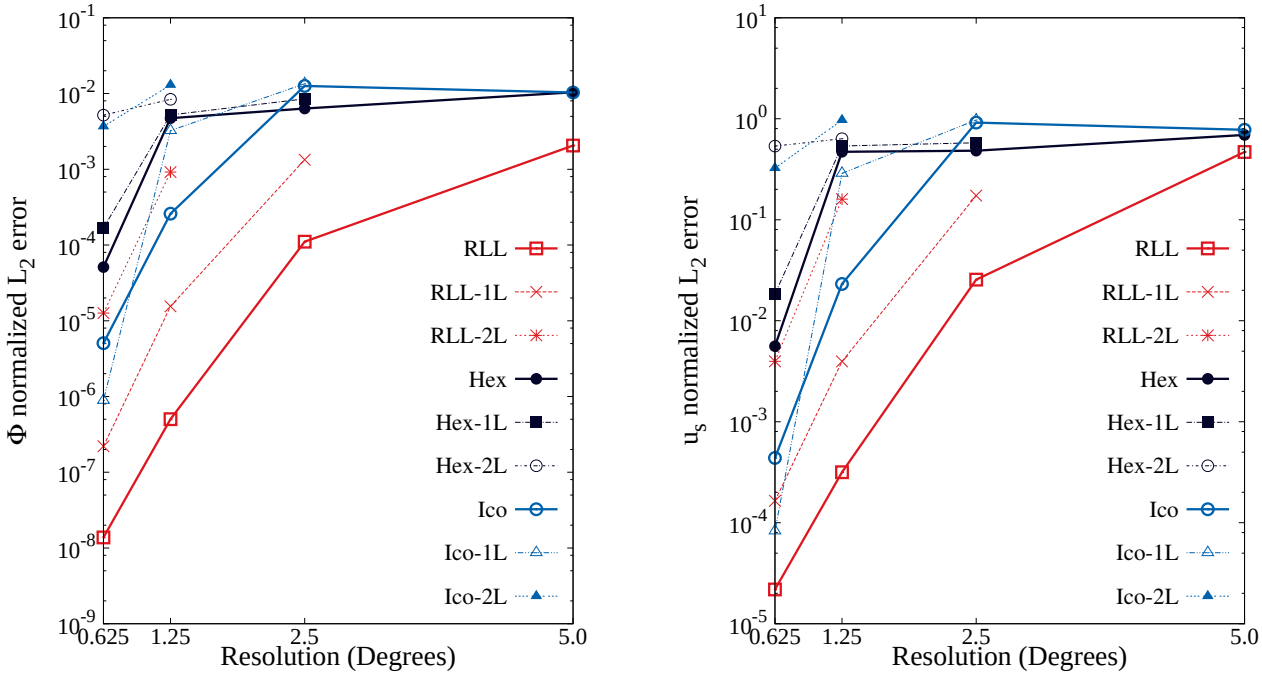

Figure 8. *Equilibrium* at day 6, inviscid: Normalized L_2 error norm of ϕ (left) and u_s (right) against the resolution measured in degrees. The error is computed with respect to the initial condition of the balanced problem on every grid. As in Fig. 7, the symbols *1L* and *2L* in the legend indicate that the solution is computed using 1 or 2 levels of refinement on non-confirming grids. In these two cases, the solution is obtained using DG, otherwise, CG is used instead. See tabulated values in the Appendix.

in atmospheric problems goes beyond the scope of this paper. Nevertheless, it should be emphasized that using an arbitrary diffusion operator may not actually improve the solution quality even though the final solution may appear smooth. This simple result stresses the importance of deriving a proper solution-based stabilization mechanism; we are working on this topic for the solution of the fully compressible Euler equations, and will report our results in a future article. For the time being, we point the reader to the recent works by Bao *et al.* (2014), Yu *et al.* (2014), Marras *et al.* (2014), and Guba *et al.* (2014).

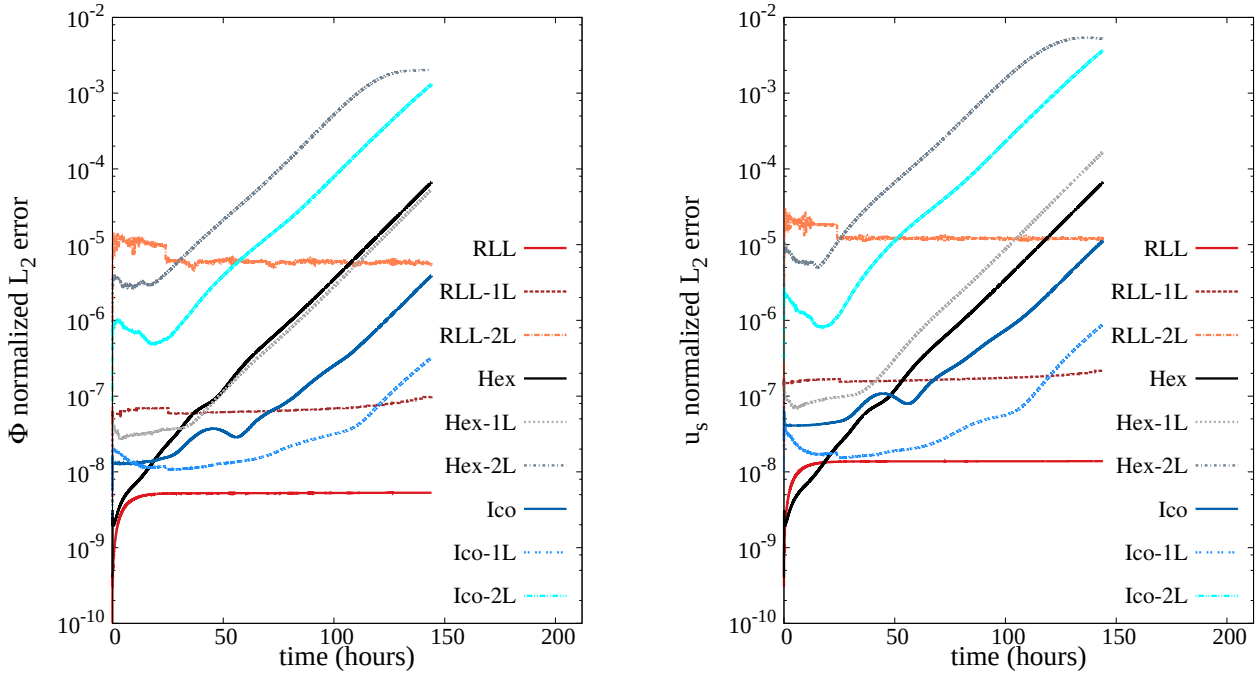

Figure 9. *Equilibrium*, inviscid: time evolution of the normalized L_2 error norm of ϕ (left) and u_s (right) relative to the initial condition computed on 100000 grid points. As for the figures above, *1L* and *2L* correspond to the DG solution on the non-conforming grids. On the other hand, the error curves *RLL, Hex* and *Ico* correspond to the CG solution on conforming grids.

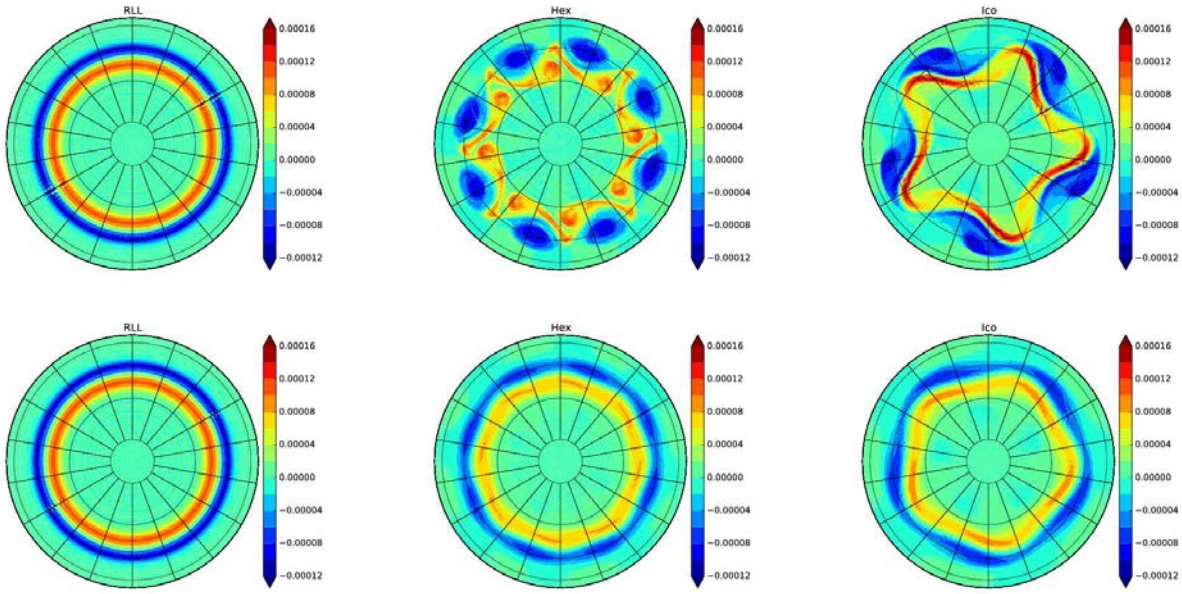

Figure 10. *Equilibrium 25000*: vorticity field (s^{-1}) at day 6, CG only. Top row: inviscid solution. Bottom row: artificial diffusion with $\nu = 1 \times 10^5 m^2\, s^{-1}$. Solution on the RLL (left), cubed-sphere (center), and icosahedral (right) grids.

5.2. *Barotropic instability*

Unlike the equilibrium problem, we do not have an analytic solution for the perturbed jet. Because of this, the solution at the highest resolution $\Delta\lambda = \Delta\varphi = 0.625°$ is considered the reference to compute the normalized errors. At this resolution, the RLL reference solution consists of 180000 grid points. Based on the analysis of the equilibrium test and the high sensitivity to the resolution in the case of the cubed-sphere and icosahedral grids, we considered the high resolution RLL run to be the true solution against which the comparison should be performed. It is a choice that is also supported by the fact that the difference between the RLL and Hex solutions first, between the Hex and Ico solutions then, and finally between the solutions on the RLL and Ico grids, are of the same order of magnitude (approximately vorticity= $O(10^{-5}\, s^{-1})$; the plots of the differences are not shown). This gives us confidence that the comparison with

Table 1. *Equilibrium: viscous vs. inviscid solution.* Normalized L_2 error norms of (ϕ, u_s, v_s) at day 6 using CG with artificial viscosity (V) $\nu = 1 \times 10^5\ \mathrm{m^2\,s^{-1}}$ on 12000 and 25000 grid points. For a direct comparison, the inviscid (I) errors computed on the same grids are also reported. *value* indicates that the use of viscosity induced an error increase in the solution. On the contrary, *value* indicates that the error norm decreased by using viscosity.

CG, L_2				
N points	12000-V	12000-I	25000-V	25000-I
RLL				
ϕ	1.493e-3	1.466e-4	1.481e-3	2.011e-5
u_s	1.575e-1	2.701e-2	1.548e-1	5.162e-3
v_s	1.575e-1	2.706e-2	1.548e-1	5.167e-3
Hex				
ϕ	3.490e-3	5.460e-3	1.744e-3	5.440e-3
u_s	3.171e-1	5.059e-1	1.814e-1	5.458e-1
v_s	3.172e-1	5.059e-1	1.815e-1	5.458e-1
Ico				
ϕ	7.002e-3	1.263e-2	3.284e-3	1.057e-2
u_s	5.762e-1	9.163e-1	2.947e-1	8.035e-1
v_s	5.762e-1	9.163e-1	2.947e-1	8.035e-1

respect to the RLL will not be biased. After 6 days, the instability has fully developed. The vorticity computed at high resolution is plotted in Fig. 11 for the three grids. There is no visible difference among the three solutions with $\Delta\varphi = \Delta\lambda \approx 0.625°$. The solutions are practically identical for $N_p \geq 25000$ (see Fig. 12). However, we see in Fig. 13 that the error increases on the cubed-sphere and Ico grid as the resolution is decreased below 25000 grid points.

Unlike for the equilibrium case, the error measures of this problem are very similar for the three different grids. This is expected because of the highly irregular structure of the jet which is no longer aligned with any grid. As the resolution is coarsened, the error is sensibly higher than its equilibrium counterpart.

In the next Section, we proceed by testing the implementation for non-conforming grids with static mesh refinement.

5.3. *Non-conforming grids*

To test the DG solver on non-conforming grids, we define a statically refined region in the proximity of the zonal wind. The high resolution static refinement is positioned within the latitude band $35° \leq \varphi_{band} \leq 55°$; this region covers approximately 10° above and below the central-line of the initial jet. Similar to the uniform case, we define a set of different equivalent grid resolutions in the banded region. We use the values $\Delta\lambda_{band} = \Delta\varphi_{band} \approx \{0.625°, 1.25°, 2.5°\}$. After fixing the resolution in this region, for each grid we add a 1-level and a 2-level global (de-)refinement. The total number of grid points in the global mesh is thus reduced. The grid structure is such that each refined region has half the resolution of its neighbors. If two refinement levels are used, and $\Delta\varphi = \Delta\lambda = 1.25°$ characterizes the finest portion of the mesh, the resolution farthest away from it has $\Delta\varphi = \Delta\lambda = 5.0°$. Based on the errors found for the coarse conforming grids, we did not go beyond this value anywhere in the domain. A total of 6 non-conforming grids are generated and are shown in Fig. 14.

It is well known that the fundamental advantage of static and dynamic grids is reflected in the lower computational cost in terms of floating point operations since the number of degrees of freedom of the grid is lower than its uniform counterpart. The normalized L_2 error norms of (ϕ, u_s, v_s) are plotted in Figs. 7 and 8 as a function of the number of points given a certain resolution in the region where most of the dynamics happen. The errors are computed for one and two refinement levels. We observe that the number of grid points necessary to obtain a certain error is reduced by adopting one level of refinement for every grid. We would expect the same to be true once the grid is further coarsened using two refinement levels, however, this is not the case in this particular instance. Due to the non-linearity of the problem and the motion of the gravity waves across the whole domain during the first hours of the simulation, the effect of the poorly resolved gravity waves in the southern hemisphere is clearly felt by the jet resolved at a finer resolution. Back to the 6-day error evolution (Fig. 9), this is clearly observed at all times. This issue should not deter us from using more than one level of refinement in general; it simply confirms the well known fact that the criterion for grid adaptation should be very well matched with the problem at hand across the entire domain.

5.4. *Dynamic grid refinement*

Both static and dynamic grid refinement are possible. Initially, a uniform and conforming grid is built before

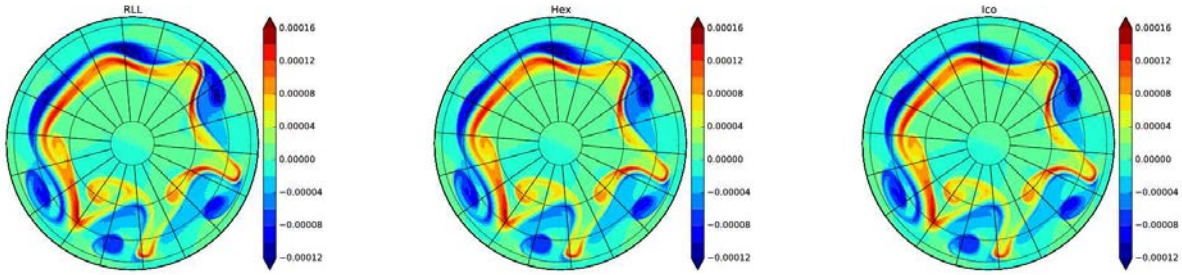

Figure 11. *Perturbed jet*: vorticity field (s^{-1}) at day 6, CG only. The flow on the RLL grid (left) the cubed-sphere (middle), and Ico grid (right) is computed with $\Delta\varphi \approx 0.625°$.

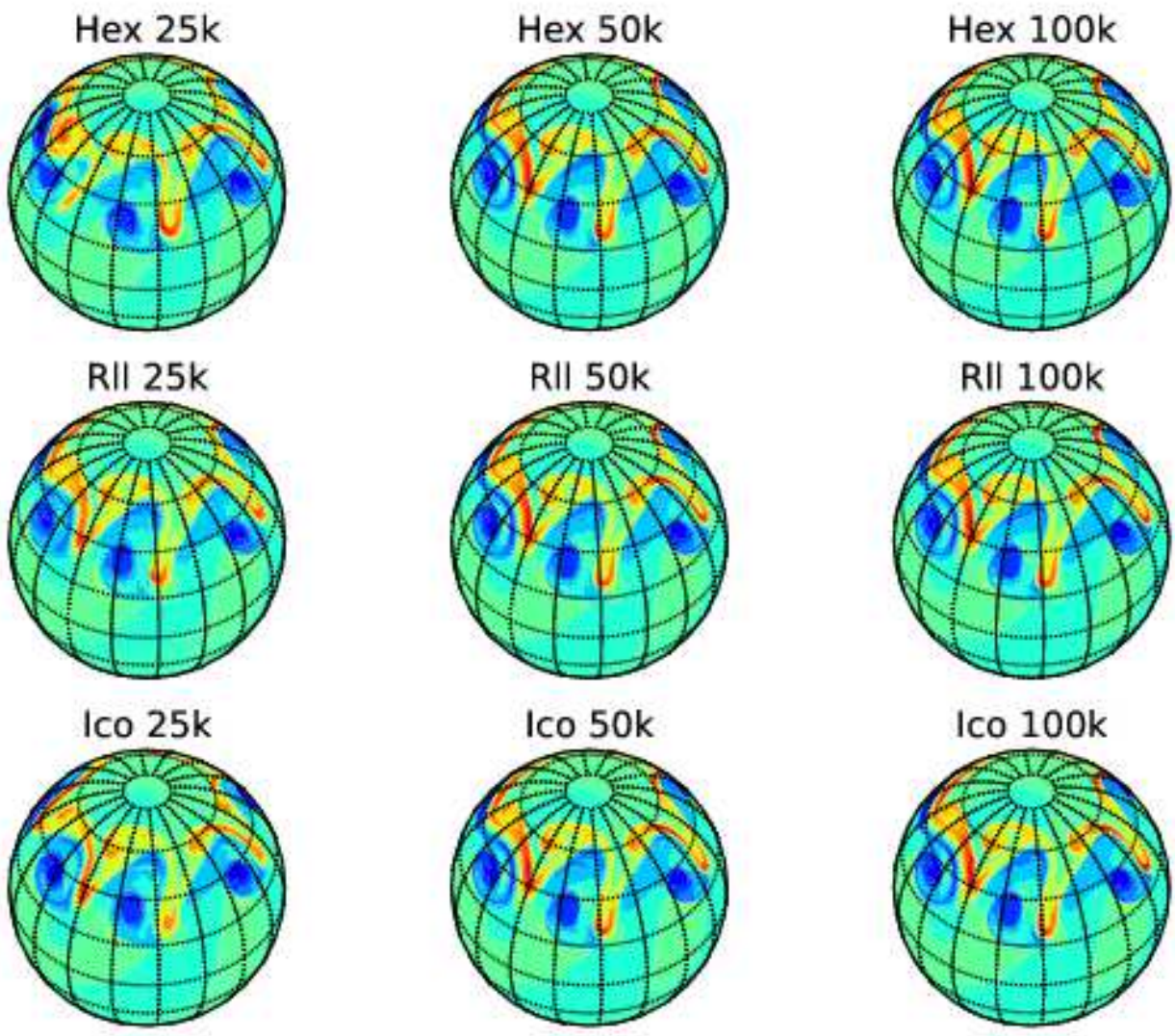

Figure 12. *Perturbed jet*, inviscid, CG only: vorticity field (s^{-1}) at day 6. Top row: Hex. Middle row: RLL. Bottom row: Ico. Solutions plotted for 25000, 50000, and 100000 grid points (from left to right). The color scale ranges between -12×10^{-5} s^{-1} (dark blue) and 16×10^{-5} s^{-1}.

proceeding to a first grid adaptation around the main jet identified by a non-zero vorticity. As the time evolves and the jet breaks, the grid is adapted according to a criterion that, in the case of this work, was chosen as the jet condition such that the vorticity $|\Lambda| < 3e-5\,s^{-1}$ (like in St-Cyr *et al.* (2008)). The initial grid configuration and the dynamically adapted grids after 6 days are shown in Fig. 15. We can state with sufficient confidence that the adaptation has performed as expected for all the grids. The jets on the three grids are highly comparable, and so are the regions of refinement and coarsening, indicating that the vorticity amplitude for the three grids is the same and corresponds to $|\Lambda| < 3e-5\,s^{-1}$.

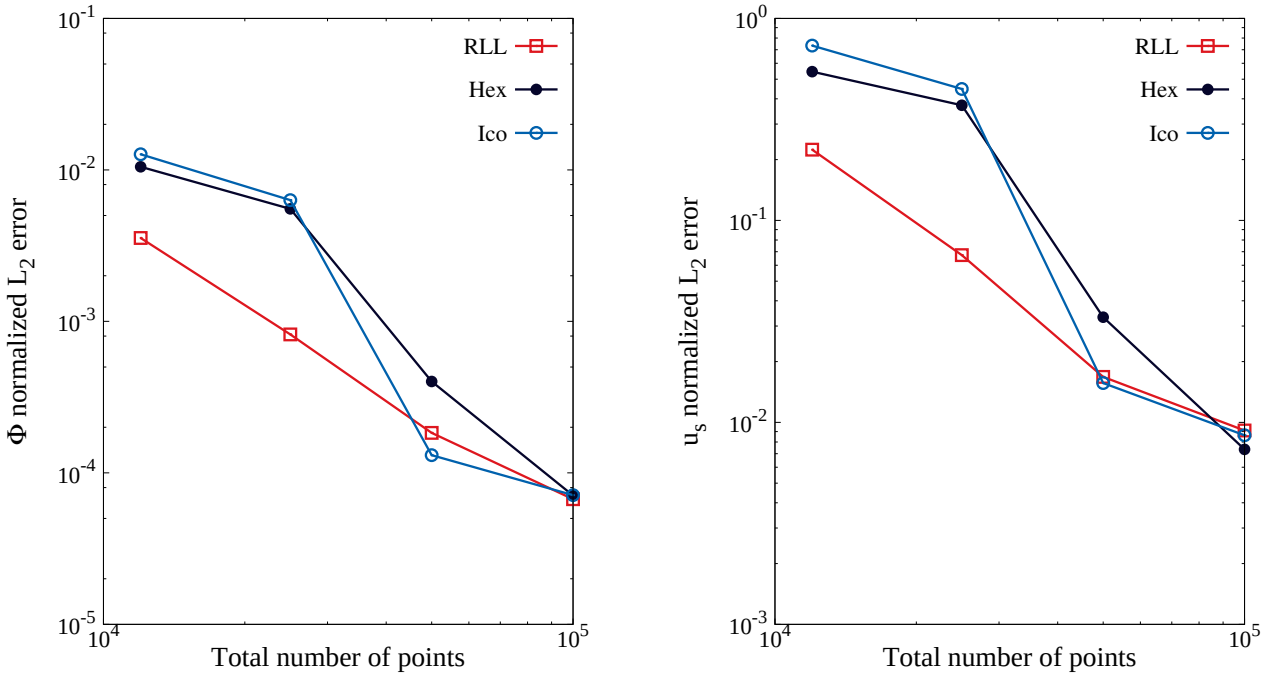

Figure 13. *Perturbed jet* at day 6, inviscid: Normalized L_2 error norms of ϕ (left) and u_s (right) against the number of grid points. The error is computed with respect to the 8^{th} order RLL solution at 0.625°, which corresponds to 180000 points. See tabulated values in the Appendix.

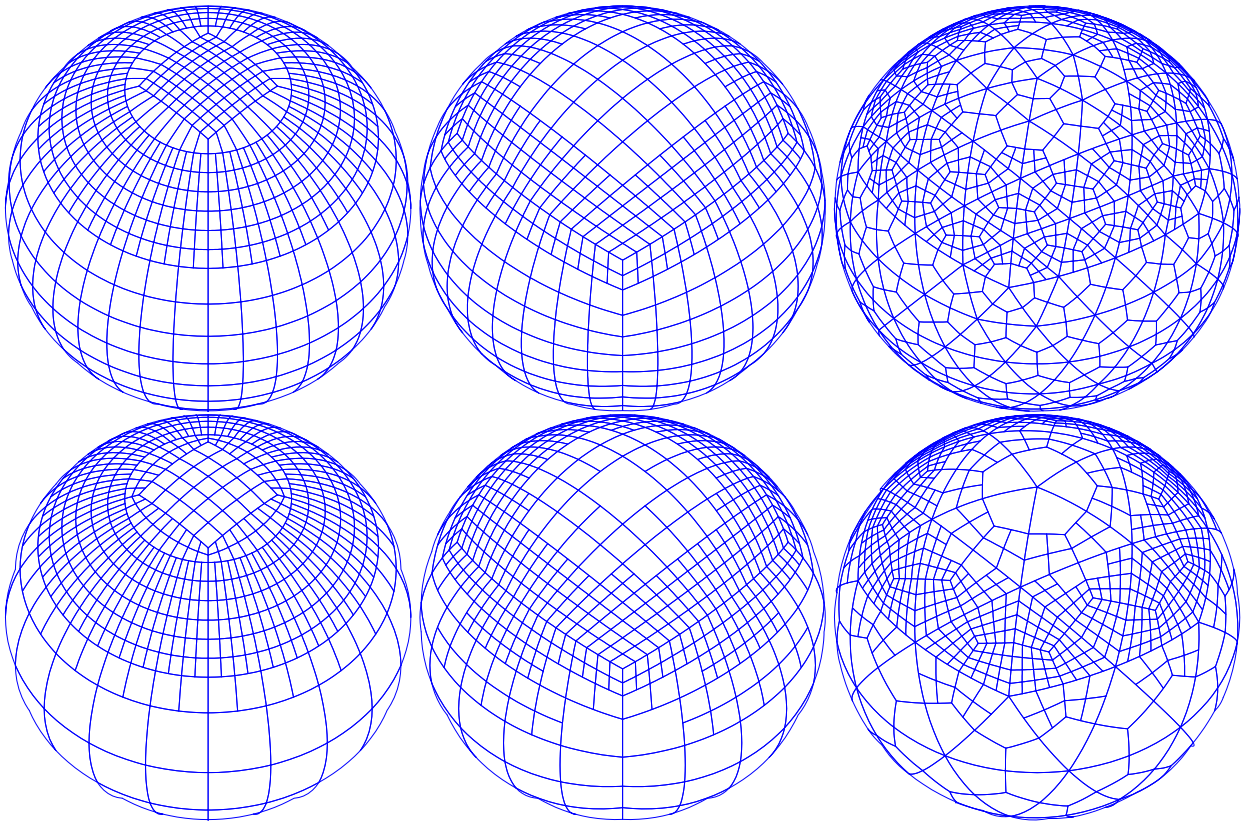

Figure 14. High-order (curved elements) non-conforming grids with 1-level (top row) and 2-level (bottom row) refinements. RLL (left column), cubed-sphere (middle column), and Ico (right column). The highest resolution in the main region of interest is $\Delta\lambda = \Delta\varphi \approx 0.625°$.

5.5. *Williamson's case 2*

To further analyze the grid effects, we run the case 2 by Williamson *et al.* (1992) which has an analytic solution. The test is run using a 45° north-wise rotation of the flow with respect to the grid with $N_p = \{25000, 50000, 100000\}$ points. For a direct comparison with St-Cyr *et al.* (2008), we also run this test using a uniform resolution of 2.5° and, additionally, of 5°. The error norms are plotted in Fig. 16. Although the steady-state solution is greatly affected by all three rotated grids, smaller error norms are found in the case of the cubed-sphere. Because 8 of the 14 patches of

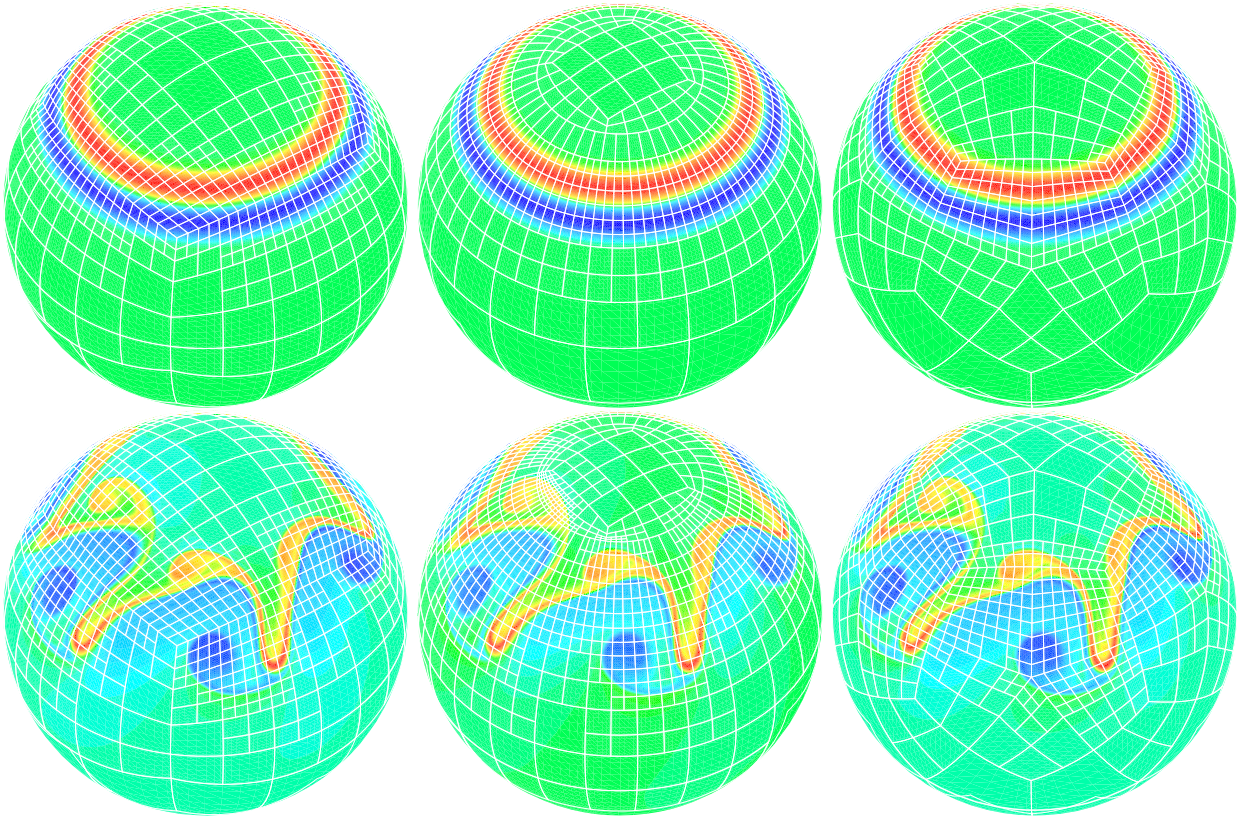

Figure 15. Dynamic grid refinement. DG solution. Top row: initial grid and vorticity field. Bottom row: adapted grid and vorticity at day 6. From left to right: cubed-sphere, RLL, icosahedral. The refinement was triggered by a vorticity value of $|\Lambda| < 3e-5\,\mathrm{s}^{-1}$.

the RLL grid are built using a linear interpolation (TFI) followed by a projection to build the high-order grid LGL points on the sphere, a series of interpolation errors seem to cause the current RLL grid to lose accuracy in the interface patches (Fig. 2). To prove this conjecture, we compute the difference between the analytic and the numerical solutions on the RLL grid and found that the larger errors are indeed concentrated on the grid points within the interface patches (plot of the difference not shown). Since the flow is not aligned in either one of the three grids, we expect that an optimized RLL grid could improve the solution to, at least, the error norms of the cubed-sphere. Nonetheless, the error norms are quantitatively comparable to the results obtained by St-Cyr *et al.* (2008).

6. Conclusions

We analyzed the behavior of a unified continuous/discontinuous element-based Galerkin model to solve the shallow water equations on six types of spherical grids. We adopted the cubed-sphere, a type of reduced Lat-Lon (RLL) grid, and the icosahedral grid in conforming, non-conforming, static, and dynamic configurations. Among others, one advantageous characteristic of element-based Galerkin methods is that they are not constrained by the logical structure of the mesh. For this reasons, it is not surprising that the spectral element and discontinuous Galerkin solutions showed almost equivalent error measures when executed in conforming mode on equivalent grids. In the case of non-conforming grids, we only showed the DG results for brevity since the CG and DG results are expected to be quite similar because the flow analyzed in this paper has no discontinuities.

To show the flexibility of our element-based Galerkin model with respect to the mesh and see how the solution may be sensitive to the grid configuration, we used two non-linear zonal flow tests. First, we solved the time-dependent geostrophic jets proposed by Galewsky *et al.* (2004). Galewsky's tests consist of (i) an unperturbed mid-latitude zonal jet on top of a geostrophically balanced geopotential height, and (ii) its perturbed counterpart where the perturbation is triggered by a bump in the geopotential. As suggested by Galewsky *et al.* (2004), both the inviscid and viscous solutions with artificial diffusion were computed.

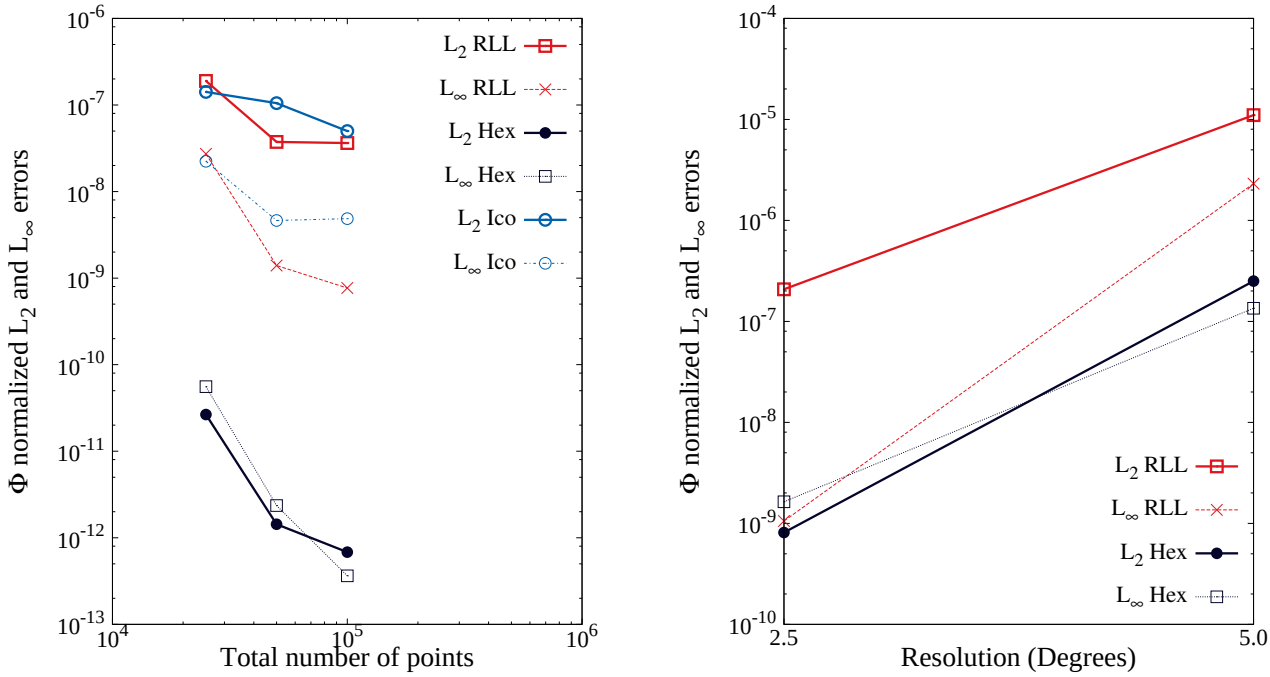

Figure 16. *Williamson's case 2.* Normalized L_2 and L_∞ errors of ϕ at day 5 using CG. Left: error against the total number of grid points. Right: error against the resolution. See tabulated values in the Appendix.

Because no exact solution exists for Galewky's tests, we also tested the code against the steady-state non-linear geostrophic flow of Williamson *et al.* (1992) which admits an analytic solution.

Although we have shown that our unified element-based Galerkin shallow water model can handle any computational grid, which implies that highly optimized arbitrary grids could be generated offline and passed onto the code without additional effort, we also found that the large problem-dependence of the solutions suggests that the users of any atmospheric model should be able to select the grid based on their knowledge of the flow to be solved.

Possibly, dynamic grid adaptivity is the real solution to always obtain a locally optimal grid configuration.

Acknowledgements

The authors gratefully acknowledge the support of the Office of Naval Research through program element PE-0602435N, the National Science Foundation (Division of Mathematical Sciences) through program element 121670, and the Air Force Office of Scientific Research through the Computational Mathematics program. The authors would like to acknowledge the Isaac Newton Institute for Mathematical Sciences at Cambridge University, UK, where part of this work was initiated during the workshop *Adaptive Multiscale Methods for the Atmosphere and Ocean*. The discussions with Dr. Hilary Weller (U. Reading, UK) on grid adaptivity in atmospheric problems is also greatly appreciated. The authors would also like to thank Dr. James F. Kelly (Exa Corp., Burlington, MA, USA) and Dr. Andreas Müller (Naval Postgraduate School) who read the manuscript and gave insightful recommendations. The work of the first and second authors was supported by the National Academies through a National Research Council fellowship. The comments by two anonymous reviewers helped improve the paper and are greatly appreciated.

A. Error tables

In this Appendix, we report the tabulated values of the error curves plotted in Figs. 7, 8, 13 for Galewsky's tests, and Fig. 16 for Williamson's test case 2.

References

Bao L, Nair RD, Tufo HM. 2014. A mass and momentum flux-form high-order discontinuous Galerkin shallow water model on the cubed-sphere. *J. Comput. Phys.* **271**: 224–243.

Boyd J. 1996. The erfc-log filter and the asymptotics of the Euler and Vandeven sequence accelerations. In: *Proc. Third Int.*

Table 4. *Equilibrium.* As table 3, but on the Ico grid. Because of the geometrical structure of Ico, the correspondence between the equivalent resolution and the number of subdivision indicated by $N6, \ldots, N1$ is not as straightforward as it is for Hex and RLL.

Geometry	*N6*	*N5*	*N4*	*N3*	*N2*	*N1*
Approximate $\Delta\lambda$	0.625°		1.25°		2.5°	5.0°
ϕ	5.064e-6	2.299e-5	2.593e-4	6.157e-3	1.261e-2	1.033e-2
u_s	4.381e-4	2.039e-3	2.313e-2	5.169e-1	9.166e-1	7.774e-1
v_s	4.381e-4	2.039e-3	2.313e-2	5.169e-1	9.166e-1	7.774e-1

Table 2. *Equilibrium.* Normalized L_2 error of (ϕ, u_s, v_s) at day 6 using CG. The error is computed with respect to the analytical initial fields given by equations (21) and (22), and is reported against the total number of grid points.

CG, L_2				
N points	100000	50000	25000	12000
RLL				
ϕ	4.878e-8	1.802e-7	2.011e-5	1.466e-4
u_s	5.910e-5	1.586e-4	5.162e-3	2.701e-2
v_s	5.910e-5	1.586e-4	5.167e-3	2.706e-2
Hex				
ϕ	6.099e-5	4.896e-4	5.440e-3	5.460e-3
u_s	6.679e-3	5.346e-2	5.458e-1	5.059e-1
v_s	6.679e-3	5.346e-2	5.458e-1	5.059e-1
Ico				
ϕ	2.230e-5	2.593e-4	1.057e-2	1.263e-2
u_s	2.040e-3	2.313e-2	8.035e-1	9.163e-1
v_s	2.040e-3	2.313e-2	8.035e-1	9.163e-1

Table 3. *Equilibrium.* As table 2, but the error is reported against the equivalent resolution $\Delta\varphi = \Delta\lambda$.

CG, L_2				
RLL	0.625°	1.25°	2.5°	5.0°
N points	180000	49000	16000	3000
ϕ	1.377e-8	5.017e-7	1.106e-4	2.056e-3
u_s	2.185e-5	3.167e-4	2.553e-2	4.694e-1
v_s	2.185e-5	3.167e-4	2.555e-2	4.694e-1
Hex	0.625°	1.25°	2.5°	5.0°
N points	124000	31000	9600	1500
ϕ	5.109e-5	4.721e-3	6.336e-3	1.038e-2
u_s	5.601e-3	4.709e-1	4.832e-1	6.918e-1
v_s	5.601e-3	4.709e-1	4.832e-1	6.918e-1

Table 5. *Equilibrium.* As in table 3, but using DG.

DG, L_2				
RLL	0.625°	1.25°	2.5°	5.0°
N points	180000	49000	16000	3000
ϕ	1.384e-8	6.556e-7	1.203e-4	2.151e-3
u_s	2.189e-5	3.261e-4	2.636e-2	4.794e-1
v_s	2.189e-5	3.260e-4	2.640e-2	4.794e-1
Hex	0.625°	1.25°	2.5°	5.0°
N points	124000	31000	9600	1500
ϕ	6.649e-5	4.948e-3	6.397e-3	1.540e-2
u_s	7.291e-3	4.933e-1	4.972e-1	9.369e-1
v_s	7.291e-3	4.933e-1	4.972e-1	9.369e-1

Table 6. Equilibrium on non-conforming grids with 1-level refinement (DG only): normalized L_2 error of (ϕ, u_s, v_s) at day 6. The error is computed with respect to the analytical initial fields given by Eqs. (21,22).

DG 1-level, L_2			
RLL-NC	0.625/1.25°	1.25/2.5°	2.5/5.0°
N points	43000	13000	5000
ϕ	2.207e-7	1.548e-5	1.337e-3
u_s	1.647e-4	3.960e-3	1.734e-1
v_s	1.647e-4	3.960e-3	1.730e-1
Hex-NC	0.625/1.25°	1.25/2.5°	2.5/5.0°
N points	31000	10000	1500
ϕ	1.680e-4	5.210e-3	8.513e-3
u_s	1.844e-2	5.372e-1	5.783e-1
v_s	1.844e-2	5.372e-1	5.783e-1
Ico-NC	0.625/1.25°	1.25/2.5°	2.5/5.0°
N points	61000	15000	4000
ϕ	8.881e-7	3.241e-3	1.348e-2
u_s	8.294e-5	2.879e-1	9.729e-1
v_s	8.294e-5	2.879e-1	9.729e-1

Table 7. As Table 6, but with 2-level refinement (DG only).

DG 2-level, L_2		
RLL-NC	0.625/1.25/2.5°	1.25/2.5/5.0°
N points	13000	5000
ϕ	1.265e-5	9.183e-4
u_s	3.964e-3	1.599e-1
v_s	3.964e-3	1.599e-1
Hex-NC	0.625/1.25/2.5°	1.25/2.5/5.0°
N points	9600	1500
ϕ	5.187e-3	8.398e-3
u_s	5.364e-1	6.348e-1
v_s	5.364e-1	6.348e-1
Ico-NC	0.625/1.25/2.5°	1.25/2.5/5.0°
N points	15000	4000
ϕ	3.670e-3	1.298e-2
u_s	3.249e-1	9.695e-1
v_s	3.249e-1	9.695e-1

Table 8. *Williamson's case 2.* Normalized L_2 and L_∞ errors of ϕ at day 5 using CG.

N points	100000	50000	25000
L_2			
Hex ϕ	6.821e-13	1.434e-12	2.650e-11
RLL ϕ	3.631e-8	3.744e-8	1.897e-7
Ico ϕ	4.997e-8	1.051e-7	1.415e-7
L_∞			
Hex ϕ	3.634e-13	2.359e-12	5.575e-11
RLL ϕ	7.693e-10	1.398e-9	2.721e-8
Ico ϕ	4.857e-9	4.633e-9	2.238e-8

Conf. Spectral and High Order Methods. Houston Journal of Mathematics, Houston, Texas. pp. 267–276.

Browning GL, Hack JJ, Swarztrauber PN. 1989. A comparison of three numerical methods for solving differential equations on the sphere. *Mon. Wea. Rev.* **117**: 1058–1075.

Cockburn B, Shu CW. 2001. Runge-kutta discontinuous Galerkin methods for convection-dominated problems. *J. of Sci.*

Table 9. *Williamson's case 2.* Normalized L_2 and L_∞ errors of ϕ at day 5 using CG with uniform resolutions of 2.5° and 5.0°.

	L_2	L_∞
2.5°		
Hex ϕ	8.109e-10	1.6353e-9
RLL ϕ	2.081e-7	1.056e-9
5°		
Hex ϕ	2.508e-7	1.348e-7
RLL ϕ	1.102e-5	2.311e-6

Computing **16**: 173–261.

Coté J. 1988. A Lagrange multiplier approach for the metric terms of semi-lagrangian models on the sphere. *Quart. J. Royal Meteor. Soc.* **114**(483): 1347–1352.

Courant R, Friedrichs K, Lewy H. 1967. On the partial difference equations of mathematical physics. *IBM Journal. English translation from the original article written in German.* **100**: 215–234.

Eriksson LE. 1984. Transfinite mesh generation and computer-aided analysis of mesh effects. PhD thesis, University of Uppsala, Sweden.

Gaberšek S, Giraldo FX, Doyle J. 2012. Dry and moist idealized experiments with a two-dimensional spectral element model. *Mon. Wea. Rev.* **140**: 3163–3182.

Galewsky J, Scott R, Polvani L. 2004. An initial-value problem for testing numerical models of the global shallow-water equations. *TELLUS* **56A**: 429–440.

Giraldo FX. 2001. A spectral element shallow water model on spherical geodesic grids. *Int. J. Num. Meth. Fluids* **35**: 869–901.

Giraldo FX, Hesthaven JS, Warburton T. 2002. Nodal high-order discontinuous Galerkin methods for spherical shallow water equations. *J. Comput. Phys.* **181**: 499–525.

Giraldo FX, Kelly JF, Constantinescu E. 2013. Implicit-explicit formulations of a three-dimensional Nonhydrostatic unified model of the atmosphere (NUMA). *SIAM J. Sci. Comput.* **35**.

Gordon WN, Hall CA. 1973. Construction of curvilinear coordinate systems and application to mesh generation. *Int. J. Numer. Methods Engrg.* **7**: 461–477.

Guba O, Taylor MA, Ullrich PA, Overfelt JR, Levy MN. 2014. The spectral element method on variable resolution grids: Evaluating grid sensitivity and resolution-aware numerical viscosity. *Geosci. Model Dev. Discuss. (submitted)* .

Hogan T, Rosmond T, Gelaro R. 1991. The nogaps forecast model: A technical description. Technical Report ADA247216, Naval Oceanographic and Atmospheric Research Lab. Monterey, CA. U.S.A.

Kelly JF, Giraldo FX. 2012. Continuous and discontinuous Galerkin methods for a scalable three-dimensional nonhydrostatic atmospheric model: Limited-area mode. *J. Comput. Phys.* **231**: 7988–8008.

Kopera MA, Giraldo FX. 2014. Analysis of adaptive mesh refinement for IMEX discontinuous Galerkin solutions of the compressible Euler equations with application to atmospheric simulations. *J. Comput. Phys. (in press)* .

Lanser D, Blom JG, Verwer JG. 2000. Spatial discretization of the shallow water equations in spherical geometry using Osher's scheme. *J. Comput. Phys.* **165**: 542–565.

Marras S, Müller A, Giraldo FX. 2014. An LES-like stabilization of the spectral element solution of the Euler equations for atmospheric flows. In: *Proceedings of the WCCM XI, ECCM V, and ECFD VI.* Barcelona, Spain.

Müller A, Behrens J, Giraldo FX, Wirth V. 2013. Comparison between adaptive and uniform discontinuous Galerkin simulations in dry 2D bubble experiments. *J. Comput. Phys.* **235**: 371–393.

Nair RD, Thomas SJ, Loft RD. 2007. A discontinuous Galerkin global shallow water model. *Mon. Wea. Rev.* **133**.

Peixoto PS, Barros SR. 2013. Analysis of grid imprinting on geodesic spherical icosahedral grids. *J. of Comput. Phys.* **237**: 61–78.

Phillips N. 1957. A map projection system suitable for large-scale numerical weather prediction. *J. Meteor. Soc. Japan* **75**: 262–267.

Qaddouri A, Pudykiewicz J, Tanguay M, Girard C, Coté J. 2012. Experiments with different discretizations for the shallow-water equations on a sphere. *Quart. J. Royal Meteor. Soc.* **138**: 989–1003.

Ronchi C, Iacono R, Paolucci PS. 1996. The Cubed Sphere: a new method for the solution of partial differential equations in spherical geometry. *J. Comput. Phys.* **124**: 93–114.

Sadourny R. 1972. Conservative finite-difference approximations of the primitive equations on quasi-uniform spherical grids. *Mon. Wea. Rev.* **100(2)**: 136–144.

Sadourny R, Arakawa A, Mintz Y. 1968. Integration of the non-divergent barotropic vorticity equation with an icosahedral-hexagonal grid for the sphere. *Mon. Wea. Rev.* **96**: 351–356.

Song C, Wolf JP. 1999. The scaled boundary finite element method –alias consistent infinitesimal finite element cell method– for diffusion. *Int. J. Numer. Methods Engrg.* **45**: 1403–1431.

Spiteri RJ, Ruuth SJ. 2002. A new class of optimal high-order strong-stability-preserving time discretization methods. *SIAM J. Numer. Anal.* **40**: 469–491.

St-Cyr A, Jablonowski C, Dennis JM, Tufo HM, Thomas SJ. 2008. A comparison of two shallow-water models with nonconforming adaptive grids. *Mon. Wea. Rev.* : 1898–1922.

Starius G. 1977. Composite mesh difference methods for elliptic and boundary value problems. *Numer. Math.* **28**: 243–258.

Taylor MA, Overfelt JR, Levy M. 2013. A variable resolution spectral element dynamical core in the Community Atmosphere

Model. Technical Report 2013-0697J, Sandia National Laboratories.

Taylor MA, Tribbia J, Iskandarani M. 1997. The spectral element method for the shallow water equations on the sphere. *J. Comput. Phys.* **130**: 92–108.

Thompson JF. 1987. A general three dimensional elliptic grid generation system on a composite block-structure. *Comput. Methods Appl. Mech. Engrg.* **64**: 377–411.

Weller H, Weller H, Fournier A. 2009. Voronoi, delaunay, and block-structured mesh refinement for solution of the shallow-water equations on the sphere. *Mon. Wea. Rev.* **137**: 4208–4224.

Williamson D, Drake J, Hack J, Jakob R, Swartztrauber P. 1992. A standard test set for numerical approximations to the shallow water equations in spherical geometry. *J. Comput. Phys.* **102**: 211–224.

Yu M, Giraldo FX, Peng M, Wang ZJ. 2014. Localized artificial viscosity stabilization of discontinuous galerkin methods for nonhydrostatic atmospheric modeling. *J. Comput. Phys. (submitted)* .

